

3D Printed Nickel-Molybdenum Based Electrocatalysts for Hydrogen Evolution at Low Overpotentials in a Flow-Through Configuration

I. Sullivan, C. Zhu, H. Zhang, M. Wood, S. Baker, C. M. Spadaccini, M. Lin, E. B. Duoss, S. Liang, C. Xiang

October 29, 2020

ACS Applied Materials and Interfaces

Disclaimer

This document was prepared as an account of work sponsored by an agency of the United States government. Neither the United States government nor Lawrence Livermore National Security, LLC, nor any of their employees makes any warranty, expressed or implied, or assumes any legal liability or responsibility for the accuracy, completeness, or usefulness of any information, apparatus, product, or process disclosed, or represents that its use would not infringe privately owned rights. Reference herein to any specific commercial product, process, or service by trade name, trademark, manufacturer, or otherwise does not necessarily constitute or imply its endorsement, recommendation, or favoring by the United States government or Lawrence Livermore National Security, LLC. The views and opinions of authors expressed herein do not necessarily state or reflect those of the United States government or Lawrence Livermore National Security, LLC, and shall not be used for advertising or product endorsement purposes.

3D Printed Nickel-Molybdenum-Based Electrocatalysts for Hydrogen Evolution at Low Overpotentials in a Flow-Through Configuration

Ian Sullivan¹, Huanlei Zhang³, Cheng Zhu², Marissa Wood², Sarah E. Baker², Christopher M. Spadaccini², Tony Van Buuren², Meng Lin³*, Eric B. Duoss²*, Siwei Liang²*, and Chengxiang Xiang¹*

Keywords: Hydrogen evolution reaction, electrocatalysis, 3D printing, alkaline electrolysis, NiMo, flow-through, electrochemistry, solar fuel

Corresponding Authors

Email: cxx@caltech.edu, liang11@llnl.gov, duoss1@llnl.gov, linm@sustech.edu.cn

¹ Liquid Sunlight Alliance (LiSA), and Department of Applied Physics and Material Science, California Institute of Technology, Pasadena, California 91125, United States

² Lawrence Livermore National Laboratory, 7000 East Avenue, Livermore, CA 94550, USA

³Department of Mechanical and Energy Engineering, Southern University of Science and Technology, Shenzhen, 518055, China

Abstract

Three dimensional (3D) printed, hierarchically porous nickel molybdenum (NiMo) electrocatalysts were synthesized and evaluated in a flow-through configuration for the hydrogen evolution reaction (HER) in 1.0 M KOH (aq.). 3D NiMo electrodes possess hierarchically porous structures owing to the resol-based aerogel precursor, which generates super-porous carbon aerogel as a catalyst support. Relative to a traditional electrode configuration, the unique flowthrough configuration allowed efficient removal of the hydrogen bubbles from the catalyst surface, especially at high operating current densities, and significantly decreased the overpotentials required for HER. An analytical model that accounted for the electro-kinetics of HER as well as the mass transport with or without the flow-through configuration was developed to quantitatively evaluate voltage losses associated with kinetic overpotentials and ohmic resistance due to bubble formation in the porous electrodes. The chemical composition and roughness factor (RF) were also systematically studied to assess the electrocatalytic performance of the 3D printed, hierarchically porous NiMo electrodes. In the flow-through configuration, a RF as high as 83,049 was obtained, and an average overpotential of 45 mV at 10 mA cm⁻² was achieved over 24 hours. The unique flow-through configuration in the 3D printed electrode provided a versatile platform for producing high surface area electrochemical electrodes for efficient fuel forming reactions.

Introduction

Hydrogen is one of the most a promising source of energy carriers for renewables and has been a focal point of clean energy research in recent years. 1-10 Photoelectrochemical (PEC) and electrochemical approaches for hydrogen production from water electrolysis have advanced significantly in terms of conversion efficiency and stability. 11 Extreme pH environment (e.g., pH=0 or pH=14) is the preferred reaction conditions for the water-splitting reaction due to the high conductivity of the electrolyte, low polarization loss associated with electrodialysis, and readily available polymer electrolyte membranes, such as cation exchange membrane (CEM) and anion exchange membrane (AEM). In the acidic condition, platinum group metals (PGMs) including Pt, Ir and Ru are the most common electrocatalysts used to produce hydrogen in commercially available electrolyzers.3,6,12-14 A main advantage of using PGMs is the low overpotential for the hydrogen evolution reaction (HER). Previous reports of ~15-80 mV overpotential ranges have been recorded for HER at relevant current densities (10 mA cm⁻²) and are attributed to favorable kinetics at the electrode surface. 15,16 Pt and IrO_x are often used as the active materials in polymer-electrolyte-membrane (PEM) electrolysis systems operating at > 1A cm⁻².¹⁷ While PGMs exhibit excellent catalytic activity for HER, the cost for these materials remains high.^{4,11} In the alkaline condition, low cost, earth-abundant materials, such as nickel molybdenum (NiMo) for HER or NiFeOx for oxygen evolution reaction (OER) exhibit excellent activity and stability. 16,18-21 In particular, NiMo alloys have shown the most promise with overpotentials <50 mV, and in some cases lower than PGMs in alkaline conditions. 1,16,29,30,20,22-28 NiMo alloys are typically formed by electrodeposition or through drop-casting of presynthesized catalyst inks onto conductive surfaces. 5,26,31 Performance of these films is highly dependent on the surface area and morphology of the electrode. For instance, hierarchically

structured surfaces result in electrodes with increased current density at a given overpotential for water splitting, due to large electrochemically active surface areas (ECSA). ^{25–28} Many reports of NiMo electrocatalysts involve deposition on flat surfaces (i.e., glassy carbon) which can limit the overall ECSA and lead to larger overpotentials while also blocking active sites due to bubble formation during HER. ^{16,24} To overcome this issue, rotating disc electrodes (RDE) are often used to probe the intrinsic electrocatalytic performance of the material. ^{32–34} By fabricating porous flow-through electrodes with large ECSAs, low overpotentials and high current densities can be achieved at high flow rates over long periods of time. ³⁵

Recently, resorcinol–formaldehyde sol–gel chemistry has proven to be an efficient approach to produce carbon aerogels with super high surface areas.³⁶ By combining versatile fabrication processes such as additive manufacturing (AM) or 3D printing with post-processing methods such as thermal activation, Chandrasekaran et al. produced 3D carbon aerogels with surface areas ~ 2000 m²/g.³⁷ In other work, Liu et al. leveraged triblock copolymer (Pluronic F127) as a sacrificial template for resol-based polymer to demonstrate ordered mesoporous carbon with high surface area.³⁸ Printable ink formulations were also developed successfully with multiple inorganic salts and multi-component metal oxides were synthesized by inkjet printing for quick screening of photocatalytic HER catalysts.³⁹

Herein, we report a 3D printed, hierarchically porous NiMo-based electrocatalyst in a flow-through configuration to dramatically increase the roughness factor (RF) and hence lower the overpotentials for HER. A record roughness factor, as high as 83,049, among reported electrochemical electrodes for HER or OER was obtained in the flow-through configuration, which can be attributed to the 3D hierarchically porous structure. Relative to a traditional planar, static electrode configuration, the flow-through configuration allowed efficient removal of

hydrogen bubbles from the catalyst surface, especially at high operating current densities, and significantly decreased the overpotentials required for HER. An analytical model that accounts for the electro-kinetics of HER as well as the mass transport with or without the flow-through configuration has been developed to quantitatively evaluate various factors for the reduced overpotentials. Bubble-induced ohmic loss accounted for most of the voltage loss at high operating current densities. We have also developed several optimization strategies to control the ink formulation and related elemental compositions of our electrochemical catalysts to reduce reaction overpotentials.

Results and Discussion

Figure 1 shows a schematic illustration of the process flow for ink formulation, 3D printing, sol-gelation, and carbonization steps to create 3D NiMo-based electrocatalysts for use in a flow-through mode. The 3D orderly structure here provided an improved mass flow control as in a flow-through configuration. The sol-gel process and the following carbonization allowed us to fabricate a hierarchically porous structure with high surface area as demonstrated by SEM images in Figure 2.

X-Ray diffraction (XRD) patterns of the prepared substrates, shown in Figure 2a, indicate mixed phases of Ni and MoO₂ for all tested compositions. At a composition of 0.68 wt.% Mo, Ni and MoO₂ peaks are present in the XRD patterns. As Mo precursor content increases to 1.8 wt.% and 3.03 wt.%, NiO and MoO₂ peaks intensify and the cubic Mo phase is observed. In addition, the Mo peaks are shifted to larger 2θ values, indicating possible Ni-Mo alloy formation or solid solutions of the oxide phases (i.e., Ni_{1-x}Mo_xO_y). ⁴⁰⁻⁴² We note that the bulk of the electrode is carbon, however, crystalline carbon phases (e.g., graphite) were not observed by XRD, which indicates the carbon is amorphous.

Rough, porous surface features and nodules were observed via scanning electron microscopy (SEM) images (Figure 2b), while energy dispersive X-ray spectroscopy (EDX) mapping revealed Mo and Ni compositions dispersed throughout the bulk of the electrode (Figure 2). Upon closer inspection of the surface, increased Ni concentration was discovered in the nodules compared to the rest of the electrode (see Supporting Information file Figure S1). While Ni and Mo elemental compositions are found to be well dispersed throughout the electrode interior, the increased Ni content of the surface nodules and existence of several phases imply phase segregation. This porous morphology resulted in large ECSAs, as well as very large

roughness factors (RF), which is the ratio of ECSA and geometric surface area (see the Supporting Information file for calculations).

Flow-through electrodes using 3D printed NiMo substrates were fabricated as detailed in the Supporting Information file (Figure S2). After immersing the electrode in 1 M KOH electrolyte, several flow rates were tested while applying 10 mA cm⁻² to the electrodes. As shown in Figure 3a, an overpotential of 60 mV was measured without electrolyte flow. The observed measurement was noisy due to the formation of H₂ gas bubbles on the surface of the electrode. As the flow started, bubbles immediately left the surface and the overpotential decreased to ~40 mV, which then slowly increased with time. Further increases in flow rate from 40 sccm to 215 sccm and from 215 sccm to 365 sccm had a much smaller impact on the overpotential of the reaction. Therefore, we used a flow rate of 215 sccm in all flow-through measurements. Linear sweep voltammetry (LSV) measurements were performed with and without flow to determine mass transport limitations of the electrodes, as shown in Figure 3b. Stark differences were observed with or without electrolyte flow, especially at high operating current densities. For example, at 500 mA cm⁻², an overpotential of -0.36 V and -0.77 V was obtained with and without flow, respectively. The flow-through electrode also allowed much higher current densities to be achieved without reaching the mass transport limiting current density. An analytical model that accounted for the electro-kinetics as well as mass transport was developed to quantitatively understand the current-voltage characteristics of the electrode with or without electrolyte flow. In the traditional electrode configuration without convective electrolyte flow, the generated hydrogen bubbles adhere to the electrode surface and reduce the ECSA for HER. In addition, the coverage of bubbles can also cause the electrolyte resistance to increase, especially operating at high current densities. As a result, the bubble coverage in the

porous electrode can directly affect the ohmic resistive loss and kinetic overpotential in the system.⁴³ We used a generalized potential partition (U) equation to account for the kinetic-overpotential (η) and the ohmic overpotentials due to electrolyte resistance (R_0) and bubble-induced resistance (R_{bubble}) :

$$U = \eta + IR_0 + IR_{\text{bubble}} \tag{1}$$

The activation overpotential η is predicted by the Tafel equation:

$$\eta = a \ln(\frac{j}{j_0(1-\Theta)}) \tag{2}$$

where a is the Tafel slope and kept as a constant of -89.47 mV based on the flow-through experimental data. The Tafel slope represents intrinsic kinetic data, which is constant for the without flow case. $j_0(1-\Theta)$ denotes the bubble-affected exchange current density. j_0 is the exchange current density of the flow-through case (-14.31 mA cm⁻² when $\Theta = 0$). For the without flow case, Θ is determined according to the operation current density, j, based on the following correlation⁴⁴:

$$\frac{j}{J_{\text{max}}} = 3.08\Theta^{1.5} (1 - \Theta)^{0.5} \tag{3}$$

where J_{max} represents the maximum current density, which is empirically chosen to correlate with the experimental data. The value of J_{max} was set to 1000 mA cm⁻² in the calculation.

In the flow-through configuration without any hydrogen bubble buildup, resistance (R_0) can be assumed to be a fixed value and equal to 0.88 Ω , and R_{bubble} is based on the experimental data, which was found to be 4.15 Ω in this study. As shown in Figure 3d, the ohmic resistive loss

becomes the dominating factor at an operating current density > ~200 mA cm² in the flow-through configuration. At 500 mA cm⁻², the kinetic overpotential increased from ~285 mV to ~310 mV due to the reduction of the ECSA when the electrolyte flow stopped, and the ohmic resistive loss due to bubble formation was ~360 mV, which accounted for the majority of the voltage drop in the traditional planar electrode configuration.

A range of chemical compositions and RFs of the porous electrodes were evaluated in the flow-through configuration at an operating current density of 10 mA cm⁻². As shown in Figure 4a, in electrodes with similar RFs, increasing the Mo content from 0.68 % to 3.03 % reduced the overpotential from 134 mV to 68 mV. The improved catalytic performance in high Mo content electrodes agrees well with previous reports. 16,31 Control experiments with 3D printed carbon electrodes (without NiMo), and flat NiMo electrodes without a flow-through configuration resulted in larger overpotentials of 524 mV and 209 mV, respectively (see Table S1). In the high Mo content electrodes, the RF of the porous electrodes was systematically varied by increasing the number of 3D printed layers or by changing the flow-through channel sizes. As shown in Figure 4b, a linear relationship between the overpotential and the Log (RF) was observed. Large RF values (as high as 83,049) were achieved in the flow-through electrodes. After observing the trends between RF and overpotential (Figure S3), we decided to perform electrochemical surface roughening by oxidizing the surface of the electrode through cyclic voltammetry (CV) in 1 M KOH. ECSA measurements were performed by CV scans (Figure S4) and a dramatic increase in the ECSA and RF was observed after oxidation (e.g., RF increased by a factor of 2.85) (Figure 4c). Chronopotentiometry (CP) measurements (Figure S5) before and after oxidation of the same electrode showed that the increased RF led to lower overpotentials at 10 mA cm⁻². XRD patterns before and after oxidation measurements are nearly identical, indicating that the phases present were not changed by electrochemical oxidation (Figure S6), therefore we attribute the decrease of overpotential to increased RF.

Figure 5 shows the overpotential at 10 mA cm⁻² as a function of time using an oxidized high Mo content porous electrode in a flow-through configuration. For the initial 12 hours, the measured overpotential was <50 mV, which gradually increased to ~ 70 mV after 24 hours as shown in Figure 5a. An average overpotential of ~45 mV was observed during this 24-hour testing period. During this period, an average H₂ Faradaic yield of 96% (±5%) was measured by gas chromatography (GC), indicating that the sole reaction was HER, with no observed side reactions (e.g., oxide reduction) (Figure 5b). The measurement was carried out for a total of 116 hours, over which time the overpotential gradually increased to 122 mV (Figure S7).

Conclusion

In summary, 3D printed, porous NiMo-based electrodes were evaluated in a flow through configuration for the hydrogen evolution reaction (HER) in 1.0 M KOH. The 3D printed electrodes exhibit uniform chemical composition with complex, multiscale interior and surface structure. As a result of their hierarchical and porous nature, the electrodes possess high surface areas and roughness factors (RFs). In electrodes with similar RFs, high Mo content electrodes exhibit the lowest overpotential at a current density of 10 mA cm⁻². The flow-through configuration efficiently removed hydrogen bubbles from the electrode surface and, hence, reduced the voltage losses associated with kinetic overpotentials and ohmic resistances, which is especially apparent at high operating current densities and when comparing against a traditional flat electrode configuration. 3D electrodes prepared without a flow-through configuration exhibit lower RF values and therefore lead to larger overpotentials for HER. The current density-voltage characteristics of the same electrode in the traditional electrode configuration and in the flowthrough electrode configuration was compared side-by-side, and the current density-voltage behavior was fitted by a multi-physics model that accounted for electro-kinetics and mass transport within the porous electrodes. The simulation results show the bubble induced resistive loss is the largest voltage loss in the traditional electrode configuration, which is especially noticeable at high current densities. Increasing the RF of the porous electrodes by increasing the number of 3D printed layers and by performing oxidative roughening further improved the electrocatalytic performance of the electrodes. A linear relationship between the overpotential at 10 mA cm⁻² and the Log (RF) was observed. In the flow-through configuration, a RF as high as 83,049 was achieved and an average overpotential of 45 mV at 10 mA cm⁻² was realized over 24 hours. This approach to create well-controlled 3D architecture combined with an advanced flowthrough configuration provides a versatile platform that could prove valuable for a broad range of high-rate electrochemical reactions.

Author Contributions

I.S. performed the electrochemical measurements, materials characterization, SEM imaging, and electrode fabrication. S.L. performed synthesis of the resin and NiMo substrates. All authors contributed to conceptualization of the research and assisted with preparing, writing, and editing the manuscript.

Associated Content

Supporting Information

Experimental methods for resin synthesis, electrode fabrication, materials characterization, electrochemical measurements, electrochemical oxidations, ECSA measurements, SEM images, EDX, XRD, and gas chromatography are provided.

Acknowledgments

The materials synthesis work at LLNL was performed under the auspices of the US Department of Energy under contract DE-AC52-07NA27344 and this work was supported by funding from LDRD award 19-SI-005 and 19-FS-047. IM review # LLNL-JRNL-816169. The characterization and analytical calculation of the flow-through electrodes are based on work performed by the Liquid Sunlight Alliance, which is supported by the U.S. Department of Energy, Office of Science, Office of Basic Energy Sciences, Fuels from Sunlight Hub under Award Number DE-SC0021266.

References

- (1) McCrory, C. C. L.; Jung, S.; Ferrer, I. M.; Chatman, S. M.; Peters, J. C.; Jaramillo, T. F. Benchmarking Hydrogen Evolving Reaction and Oxygen Evolving Reaction Electrocatalysts for Solar Water Splitting Devices. *J. Am. Chem. Soc.* **2015**, *137* (13), 4347–4357. https://doi.org/10.1021/ja510442p.
- (2) Lewis, N. S.; Nocera, D. G. Powering the Planet: Chemical Challenges in Solar Energy Utilization. *Proc. Natl. Acad. Sci.* **2006**, *103* (43), 15729–15735. https://doi.org/10.1073/pnas.0603395103.
- (3) Cheng, N.; Stambula, S.; Wang, D.; Banis, M. N.; Liu, J.; Riese, A.; Xiao, B.; Li, R.; Sham, T. K.; Liu, L. M.; et al. Platinum Single-Atom and Cluster Catalysis of the Hydrogen Evolution Reaction. *Nat. Commun.* **2016**, *7*, 1–9. https://doi.org/10.1038/ncomms13638.
- (4) Eftekhari, A. Electrocatalysts for Hydrogen Evolution Reaction. *Int. J. Hydrogen Energy* **2017**, *42* (16), 11053–11077. https://doi.org/10.1016/j.ijhydene.2017.02.125.
- (5) Gong, M.; Wang, D.; Chen, C.; Hwang, B.; Dai, H. A Mini Review on Nickel-Based Electrocatalysts for Alkaline Hydrogen Evolution Reaction. *Nano Res.* **2016**, *9* (1), 28–46. https://doi.org/10.1007/s12274-015-0965-x.
- (6) Grigoriev, S. A.; Millet, P.; Fateev, V. N. Evaluation of Carbon-Supported Pt and Pd Nanoparticles for the Hydrogen Evolution Reaction in PEM Water Electrolysers. *J. Power Sources* **2008**, *177* (2), 281–285. https://doi.org/10.1016/j.jpowsour.2007.11.072.
- (7) Jiang, S.; Zhang, R.; Liu, H.; Rao, Y.; Yu, Y.; Chen, S.; Yue, Q.; Zhang, Y.; Kang, Y. Promoting Formation of Oxygen Vacancies in Two-Dimensional Cobalt-Doped Ceria Nanosheets for Efficient Hydrogen Evolution. *J. Am. Chem. Soc.* **2020**, *142* (14), 6461–6466. https://doi.org/10.1021/jacs.9b13915.
- (8) Liu, E.; Li, J.; Jiao, L.; Doan, H. T. T.; Liu, Z.; Zhao, Z.; Huang, Y.; Abraham, K. M.; Mukerjee, S.; Jia, Q. Unifying the Hydrogen Evolution and Oxidation Reactions Kinetics in Base by Identifying the Catalytic Roles of Hydroxyl-Water-Cation Adducts. *J. Am. Chem. Soc.* **2019**, *141* (7), 3232–3239. https://doi.org/10.1021/jacs.8b13228.
- (9) Mahmood, N.; Yao, Y.; Zhang, J.-W.; Pan, L.; Zhang, X.; Zou, J.-J. Electrocatalysts for Hydrogen Evolution in Alkaline Electrolytes: Mechanisms, Challenges, and Prospective Solutions. *Adv. Sci.* **2018**, *5* (2), 1700464. https://doi.org/10.1002/advs.201700464.
- (10) Zheng, Y.; Jiao, Y.; Vasileff, A.; Qiao, S. The Hydrogen Evolution Reaction in Alkaline Solution: From Theory, Single Crystal Models, to Practical Electrocatalysts. *Angew. Chemie Int. Ed.* **2018**, *57* (26), 7568–7579. https://doi.org/10.1002/anie.201710556.
- (11) Ramaswamy, N.; Mukerjee, S. Alkaline Anion-Exchange Membrane Fuel Cells: Challenges in Electrocatalysis and Interfacial Charge Transfer. *Chem. Rev.* **2019**, *119* (23), 11945–11979. https://doi.org/10.1021/acs.chemrev.9b00157.
- (12) Jiang, P.; Yang, Y.; Shi, R.; Xia, G.; Chen, J.; Su, J.; Chen, Q. Pt-like Electrocatalytic Behavior of Ru-MoO₂ Nanocomposites for the Hydrogen Evolution Reaction. *J. Mater.*

- Chem. A **2017**, 5 (11), 5475–5485. https://doi.org/10.1039/c6ta09994g.
- (13) Stamenkovic, V. R.; Strmcnik, D.; Lopes, P. P.; Markovic, N. M. Energy and Fuels from Electrochemical Interfaces. *Nat. Mater.* **2017**, *16* (1), 57–69. https://doi.org/10.1038/nmat4738.
- (14) Yu, J.; Guo, Y.; She, S.; Miao, S.; Ni, M.; Zhou, W.; Liu, M.; Shao, Z. Bigger Is Surprisingly Better: Agglomerates of Larger RuP Nanoparticles Outperform Benchmark Pt Nanocatalysts for the Hydrogen Evolution Reaction. *Adv. Mater.* **2018**, *30* (39), 1–10. https://doi.org/10.1002/adma.201800047.
- (15) Wu, Q.; Luo, M.; Han, J.; Peng, W.; Zhao, Y.; Chen, D.; Peng, M.; Liu, J.; de Groot, F. M. F.; Tan, Y. Identifying Electrocatalytic Sites of the Nanoporous Copper–Ruthenium Alloy for Hydrogen Evolution Reaction in Alkaline Electrolyte. ACS Energy Lett. 2020, 5 (1), 192–199. https://doi.org/10.1021/acsenergylett.9b02374.
- (16) McKone, J. R.; Sadtler, B. F.; Werlang, C. A.; Lewis, N. S.; Gray, H. B. Ni–Mo Nanopowders for Efficient Electrochemical Hydrogen Evolution. *ACS Catal.* **2013**, *3* (2), 166–169. https://doi.org/10.1021/cs300691m.
- (17) Xu, D.; Stevens, M. B.; Cosby, M. R.; Oener, S. Z.; Smith, A. M.; Enman, L. J.; Ayers, K. E.; Capuano, C. B.; Renner, J. N.; Danilovic, N.; et al. Earth-Abundant Oxygen Electrocatalysts for Alkaline Anion-Exchange-Membrane Water Electrolysis: Effects of Catalyst Conductivity and Comparison with Performance in Three-Electrode Cells. ACS Catal. 2019, 9 (1), 7–15. https://doi.org/10.1021/acscatal.8b04001.
- (18) Lu, X.; Zhao, C. Electrodeposition of Hierarchically Structured Three-Dimensional Nickel–Iron Electrodes for Efficient Oxygen Evolution at High Current Densities. *Nat. Commun.* **2015**, *6* (1), 6616. https://doi.org/10.1038/ncomms7616.
- (19) McCrory, C. C. L.; Jung, S.; Peters, J. C.; Jaramillo, T. F. Benchmarking Heterogeneous Electrocatalysts for the Oxygen Evolution Reaction. *J. Am. Chem. Soc.* **2013**, *135* (45), 16977–16987. https://doi.org/10.1021/ja407115p.
- (20) Zhou, Y.; Luo, M.; Zhang, W.; Zhang, Z.; Meng, X.; Shen, X.; Liu, H.; Zhou, M.; Zeng, X. Topological Formation of a Mo-Ni-Based Hollow Structure as a Highly Efficient Electrocatalyst for the Hydrogen Evolution Reaction in Alkaline Solutions. *ACS Appl. Mater. Interfaces* **2019**. https://doi.org/10.1021/acsami.9b03686.
- (21) Zeng, M.; Li, Y. Recent Advances in Heterogeneous Electrocatalysts for the Hydrogen Evolution Reaction. *J. Mater. Chem. A* **2015**, *3* (29), 14942–14962. https://doi.org/10.1039/c5ta02974k.
- (22) Zhang, J.; Wang, T.; Liu, P.; Liao, Z.; Liu, S.; Zhuang, X.; Chen, M.; Zschech, E.; Feng, X. Efficient Hydrogen Production on MoNi₄ Electrocatalysts with Fast Water Dissociation Kinetics. *Nat. Commun.* **2017**, 8 (May), 1–8. https://doi.org/10.1038/ncomms15437.
- (23) Chen, W.; Sasaki, K.; Ma, C.; Frenkel, A. I.; Marinkovic, N.; Muckerman, J. T.; Zhu, Y.; Adzic, R. R. Hydrogen-Evolution Catalysts Based on Non-Noble Metal Nickel-Molybdenum Nitride Nanosheets. *Angew. Chemie Int. Ed.* **2012**, *51* (25), 6131–6135. https://doi.org/10.1002/anie.201200699.

- (24) Fan, C.; Piron, D. L.; Sleb, A.; Paradis, P. Study of Electrodeposited Nickel-Molybdenum, Cobalt-Tungsten as Hydrogen Electrodes in Alkaline Water Electrolysis. *J. Ele* **1994**, *141* (2), 382–387.
- (25) Fang, M.; Gao, W.; Dong, G.; Xia, Z.; Yip, S.; Qin, Y.; Qu, Y.; Ho, J. C. Hierarchical NiMo-Based 3D Electrocatalysts for Highly-Efficient Hydrogen Evolution in Alkaline Conditions. *Nano Energy* **2016**, *27*, 247–254. https://doi.org/10.1016/j.nanoen.2016.07.005.
- (26) Gao, W.; Gou, W.; Zhou, X.; Ho, J. C.; Ma, Y.; Qu, Y. Amine-Modulated/Engineered Interfaces of NiMo Electrocatalysts for Improved Hydrogen Evolution Reaction in Alkaline Solutions. *ACS Appl. Mater. Interfaces* **2018**, *10* (2), 1728–1733. https://doi.org/10.1021/acsami.7b16125.
- (27) Ito, Y.; Ohto, T.; Hojo, D.; Wakisaka, M.; Nagata, Y.; Chen, L.; Hu, K.; Izumi, M.; Fujita, J.; Adschiri, T. Cooperation between Holey Graphene and NiMo Alloy for Hydrogen Evolution in an Acidic Electrolyte. ACS Catal. 2018, 8 (4), 3579–3586. https://doi.org/10.1021/acscatal.7b04091.
- (28) Liu, Z.; Zhang, G.; Bu, J.; Ma, W.; Yang, B.; Zhong, H.; Li, S.; Wang, T.; Zhang, J. Single-Crystalline Mo-Nanowire-Mediated Directional Growth of High-Index-Faceted MoNi Electrocatalyst for Ultralong-Term Alkaline Hydrogen Evolution. *ACS Appl. Mater. Interfaces* **2020**, *12* (32), 36259–36267. https://doi.org/10.1021/acsami.0c11716.
- (29) Pehlivan, İ. B.; Arvizu, M. A.; Qiu, Z.; Niklasson, G. A.; Edvinsson, T. Impedance Spectroscopy Modeling of Nickel–Molybdenum Alloys on Porous and Flat Substrates for Applications in Water Splitting. *J. Phys. Chem. C* **2019**, *123* (39), 23890–23897. https://doi.org/10.1021/acs.jpcc.9b02714.
- (30) Ling, T.; Zhang, T.; Ge, B.; Han, L.; Zheng, L.; Lin, F.; Xu, Z.; Hu, W.; Du, X.; Davey, K.; et al. Well-Dispersed Nickel- and Zinc-Tailored Electronic Structure of a Transition Metal Oxide for Highly Active Alkaline Hydrogen Evolution Reaction. *Adv. Mater.* **2019**, *31* (16), 1807771. https://doi.org/10.1002/adma.201807771.
- (31) Navarro-Flores, E.; Chong, Z.; Omanovic, S. Characterization of Ni, NiMo, NiW and NiFe Electroactive Coatings as Electrocatalysts for Hydrogen Evolution in an Acidic Medium. *J. Mol. Catal. A Chem.* **2005**, 226 (2), 179–197. https://doi.org/10.1016/j.molcata.2004.10.029.
- (32) Arminio-Ravelo, J. A.; Jensen, A. W.; Jensen, K. D.; Quinson, J.; Escudero-Escribano, M. Electrolyte Effects on the Electrocatalytic Performance of Iridium-Based Nanoparticles for Oxygen Evolution in Rotating Disc Electrodes. *ChemPhysChem* **2019**, *20* (22), 2956–2963. https://doi.org/10.1002/cphc.201900902.
- (33) Mayrhofer, K. J. J.; Strmcnik, D.; Blizanac, B. B.; Stamenkovic, V.; Arenz, M.; Markovic, N. M. Measurement of Oxygen Reduction Activities via the Rotating Disc Electrode Method: From Pt Model Surfaces to Carbon-Supported High Surface Area Catalysts. *Electrochim. Acta* 2008, 53 (7), 3181–3188. https://doi.org/10.1016/j.electacta.2007.11.057.
- (34) Zhu, P.; Zhao, Y. Effects of Electrochemical Reaction and Surface Morphology on

- Electroactive Surface Area of Porous Copper Manufactured by Lost Carbonate Sintering. *RSC Adv.* **2017**, *7* (42), 26392–26400. https://doi.org/10.1039/c7ra04204c.
- (35) Yang, F.; Kim, M. J.; Brown, M.; Wiley, B. J. Alkaline Water Electrolysis at 25 A Cm⁻² with a Microfibrous Flow-through Electrode. *Adv. Energy Mater.* **2020**, *10* (25), 1–10. https://doi.org/10.1002/aenm.202001174.
- (36) Baumann, T. F.; Worsley, M. A.; Han, T. Y. J.; Satcher, J. H. High Surface Area Carbon Aerogel Monoliths with Hierarchical Porosity. *J. Non. Cryst. Solids* **2008**, *354* (29), 3513–3515. https://doi.org/10.1016/j.jnoncrysol.2008.03.006.
- (37) Chandrasekaran, S.; Yao, B.; Liu, T.; Xiao, W.; Song, Y.; Qian, F.; Zhu, C.; Duoss, E. B.; Spadaccini, C. M.; Li, Y.; et al. Direct Ink Writing of Organic and Carbon Aerogels. *Mater. Horizons* **2018**, *5* (6), 1166–1175. https://doi.org/10.1039/c8mh00603b.
- (38) Liu, R.; Shi, Y.; Wan, Y.; Meng, Y.; Zhang, F.; Gu, D.; Chen, Z.; Tu, B.; Zhao, D. Triconstituent Co-Assembly to Ordered Mesostructured Polymer-Silica and Carbon-Silica Nanocomposites and Large-Pore Mesoporous Carbons with High Surface Areas. *J. Am. Chem. Soc.* **2006**, *128* (35), 11652–11662. https://doi.org/10.1021/ja0633518.
- (39) Liu, X.; Shen, Y.; Yang, R.; Zou, S.; Ji, X.; Shi, L.; Zhang, Y.; Liu, D.; Xiao, L.; Zheng, X.; et al. Inkjet Printing Assisted Synthesis of Multicomponent Mesoporous Metal Oxides for Ultrafast Catalyst Exploration. *Nano Lett.* **2012**, *12* (11), 5733–5739. https://doi.org/10.1021/nl302992q.
- (40) Shang, P.; Ye, Z.; Ding, Y.; Zhu, Z.; Peng, X.; Ma, G.; Li, D. Nanosponge-like Solid Solution of NiMo with a High Hydrogen Evolution Reaction Performance over a Wide Range of Current Densities. *ACS Sustain. Chem. Eng.* **2020**, 8 (29), 10664–10672. https://doi.org/10.1021/acssuschemeng.0c00783.
- (41) Nairan, A.; Zou, P.; Liang, C.; Liu, J.; Wu, D.; Liu, P.; Yang, C. NiMo Solid Solution Nanowire Array Electrodes for Highly Efficient Hydrogen Evolution Reaction. *Adv. Funct. Mater.* **2019**, *29* (44), 1–8. https://doi.org/10.1002/adfm.201903747.
- (42) Liu, J. H.; Pei, Z. L.; Shi, W. B.; Liu, Y. D.; Gong, J.; Sun, C. Studies on Preparation, Microstructure, Mechanical Properties and Corrosion Resistance of Ni[Sbnd]Mo/Micron-Sized Diamond Composite Coatings. *Surf. Coatings Technol.* **2020**, *385* (February), 125451. https://doi.org/10.1016/j.surfcoat.2020.125451.
- (43) Angulo, A.; van der Linde, P.; Gardeniers, H.; Modestino, M.; Fernández Rivas, D. Influence of Bubbles on the Energy Conversion Efficiency of Electrochemical Reactors. *Joule* **2020**, *4* (3), 555–579. https://doi.org/10.1016/j.joule.2020.01.005.
- (44) Vogt, H. The Quantities Affecting the Bubble Coverage of Gas-Evolving Electrodes. *Electrochim. Acta* **2017**, *235*, 495–499. https://doi.org/10.1016/j.electacta.2017.03.116.

Material	Overpotential	Electrolyte	Stability	Roughness	Flow	Reference
	(mV) 10 mA cm ⁻²		(h)	Factor	Through	
MoNi ₄	15	1 M KOH	10	18500	No	22
Mo@MoNi	18	1 M KOH	1680	3722	No	28
NiMo	30	1 M KOH	20	735	No	25
Ni-Zn-CoO	53	6 M KOH	24	N/A	No	30
NiMo Nanopowder	70	2 M KOH	96	130	No	16
Mo-Ni	38	1 M KOH	10	N/A	No	20
NiMo (a)	30	1 M NaOH	24	800	No	1
NiMo (b)	130	1 M NaOH	24	1000	No	1
NiMoCo	110	1 M NaOH	24	900	No	1
NiMoFe (a)	130	1 M NaOH	24	900	No	1
NiFe	120	1 M NaOH	24	4000	No	1
Amine Modulated	72	1 M KOH	N/A	N/A	No	26
NiMo						
3D Printed NiMo	45	1 M KOH	24	83049	Yes	This work
(High Mo)						

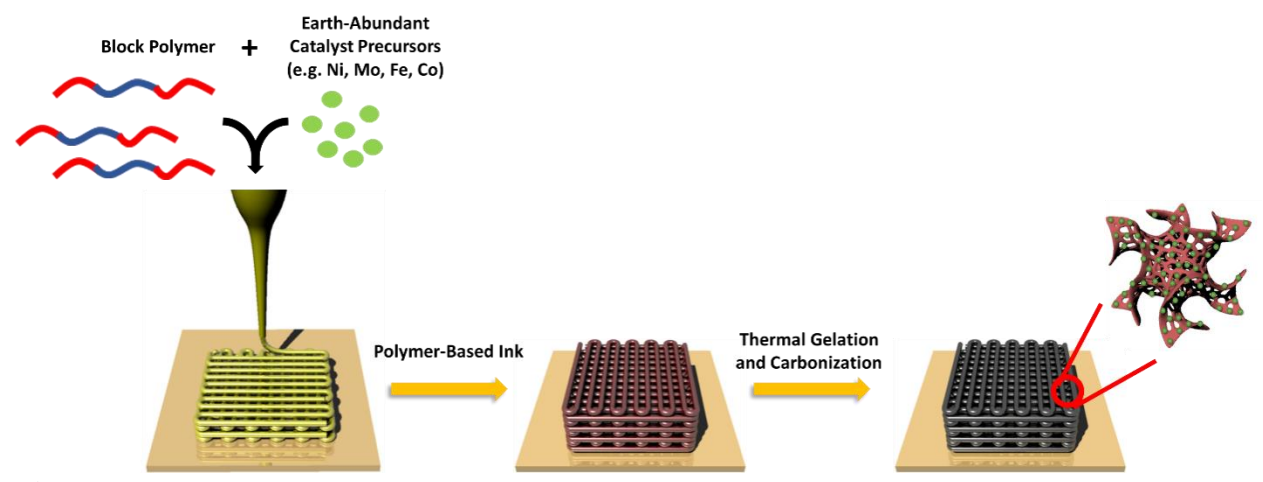


Figure 1. A schematic illustration of the process flow to produce 3D NiMo-based electrocatalysts.

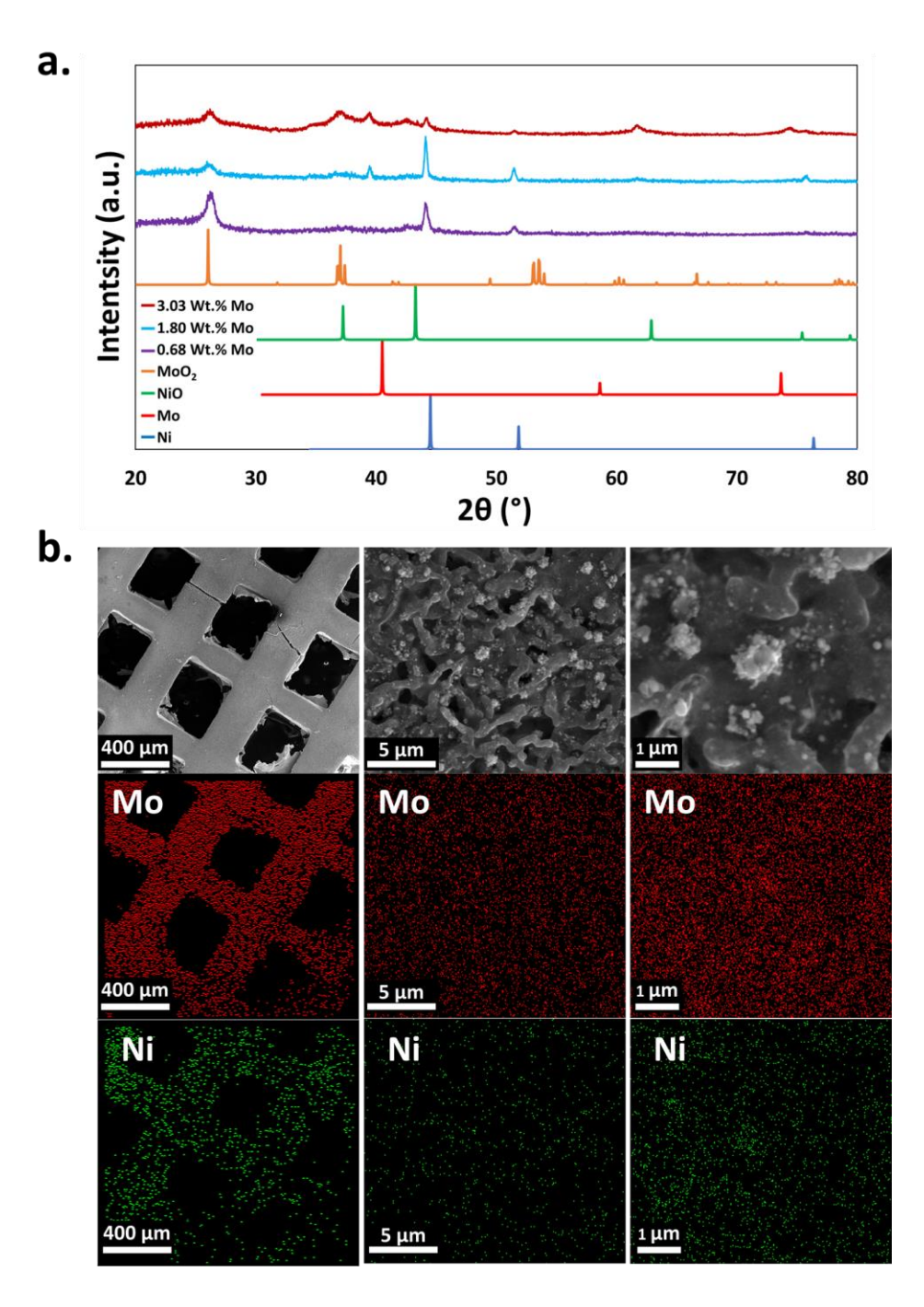


Figure 2. (a) XRD patterns and (b) SEM/EDS of the 3D printed, porous NiMo electrodes.

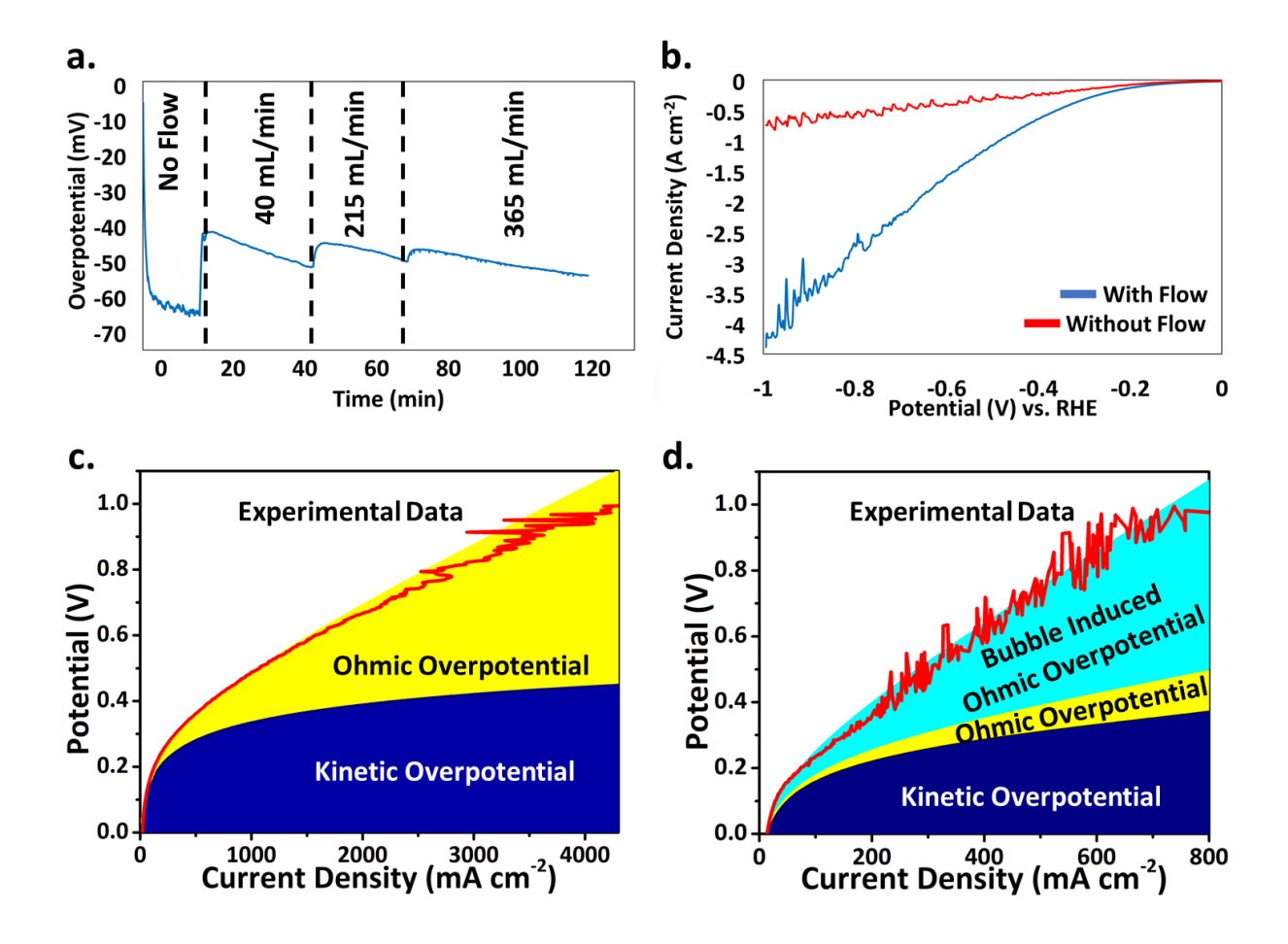


Figure 3. (a) Impact of flow rate on the overpotential of the 3D printed, porous electrodes at 10 mA cm⁻² as a function of time. (b) The current density-voltage characteristics of the porous NiMo electrodes in a traditional electrode configuration (red) and in a flow-through configuration (blue). (c)The simulated contribution from kinetic overpotential and ohmic resistive loss in the flow-through configuration, and (d) simulated contribution from kinetic overpotential, ohmic resistive loss and additional bubble induced ohmic resistive loss in the traditional electrode configuration. The experimental data curves in (c) and (d) are the experimental measurements from (b).

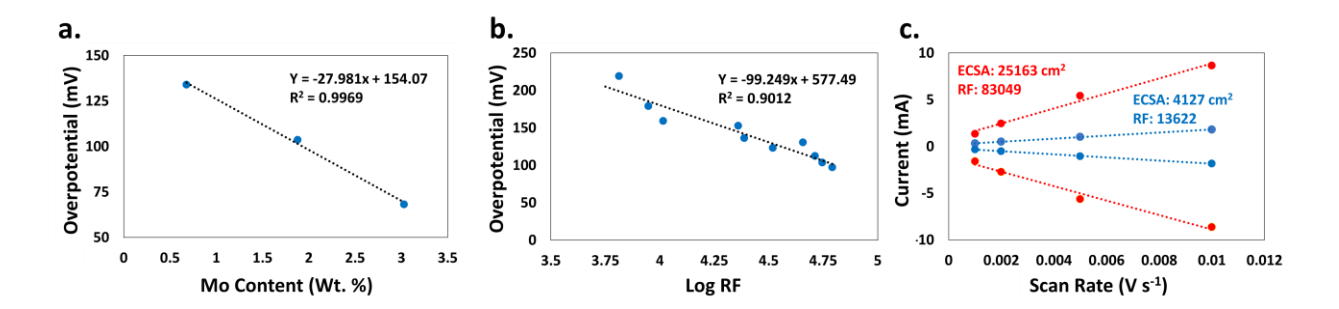


Figure 4. (a) Overpotential at 10 mA cm⁻² as a function of Mo content. RF values for these electrodes are similar (see Table S1.) (b) Correlation between RFs and overpotential at 10 mA cm⁻² (c) ECSA and RF values before (blue) and after (red) electrochemical oxidation.

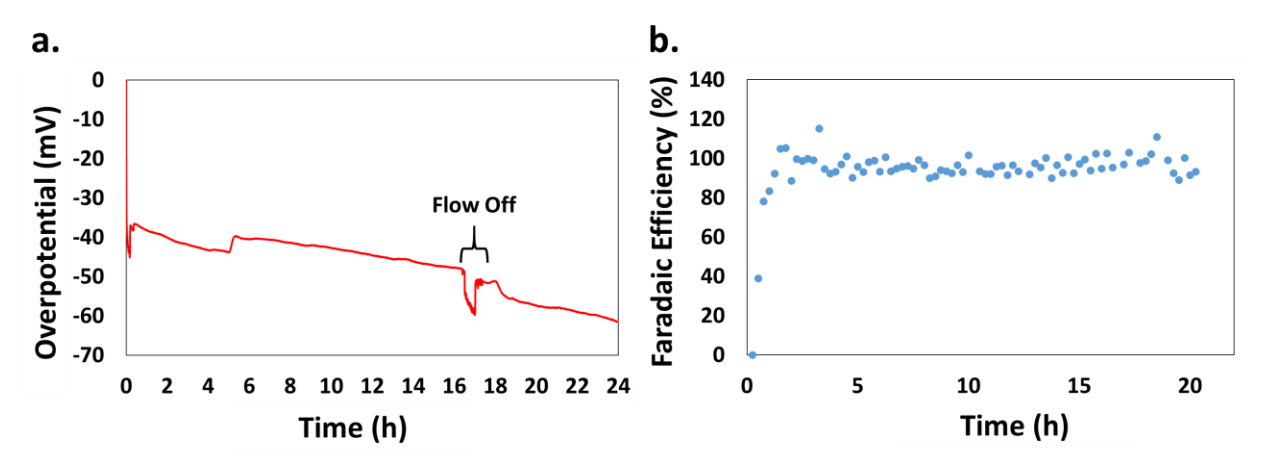


Figure 5. (a) Chronopotentiometry (CP) measurements of NiMo electrode at 10 mA cm⁻² for 24 hours, and (b) the corresponding Faradaic efficiency for hydrogen.